Preprints of the 19th World Congress
The International Federation of Automatic Control
Cape Town, South Africa. August 24-29, 2014

Model-based PID control of a Dielectric Electro-Active Polymer Positioning System

Rizzello G.*, Naso D. *, York. A., Seelecke S.****

** Politecnico di Bari, Department of Electrical Engineering and Electronics, Italy (e-mail: naso@poliba.it).*
*** Saarland University, Department of Mechatronics, Saarbrücken, Germany (e-mail: stefan.seelecke@mmsl.uni-saarland.de).*

Abstract: This paper considers a micrometric positioning system based on a dielectric electro-active polymer membrane. The motion is generated by the deformation of the membrane caused by the electrostatic compressive force between two compliant electrodes applied on the surface of the polymer. The paper suggests various model-based design strategies (in both time and frequency domains) for PID control laws, which are able to compensate the nonlinear behavior of the actuator (caused by the characteristics of the material and the annular geometry of the membrane) and obtain very precise tracking of steps or sinusoidal reference signals. The various design strategies are discussed and compared both in simulations and experiments.

Keywords: Dielectric ElectroActive Polymer, Diaphragm Actuators, Physical Models, Parameter Identification, Position Control, PID Control, Robust Control.

1. INTRODUCTION

Smart materials such as piezoelectric ceramics, magnetostrictives, thermal or magnetic shape memory alloys (MSMA) have shown to be effective in achieving increased accuracy, efficiency and lightweight standards in many application fields, ranging from positioning systems to vibration dampers and energy harvesters. Electro-Active Polymers (EAP) are a younger class of promising smart material that react to electrical or chemical stimuli with a deformation of their shape, which in some cases can be several orders of magnitude higher than the one of state-of-art piezoelectric ceramics. Dielectric EAP (DEAP) are a specific type of EAP in which actuation is generated by the combination of the elasticity of the polymer with the compressive electrostatic forces between compliant electrodes applied on the surface of the material. DEAP are attractive because of their lightweight, high energy density, fast response and low costs. Prototypes of DEAP pumps (Loverich et al. (2006)), valves (Giousouf & Kovacs (2013)), robots (Plante (2006)), and micropositioning stages (Jordan et al. (2011)) have been documented in recent literature. On the other hand, there are many technological issues that still need to be properly addressed, such as the demand of voltage needed to obtain the deformation, the dependence of the DEAP membrane from the temperature and fatigue. The design of feedback control systems is a possible way to partly overcome these limitations. However, most of the recent research efforts on DEAP focus on material static and dynamic characterization (Plante & Dubowsky (2007), York et al. (2010), Hodgins et al. (2011)), and accurate analysis of the underlying physical phenomena (Hackl et al. (2005), Wissler & Mazza (2007), Kaal & Herold (2011), Berselli et al. (2012), Hodgins et al. (2013), Rizzello et al. (2013a)), while the investigation about the effects of feedback control is considered less frequently (see, e.g., Xie et al. (2005), Randazzo et al. (2010), Sarban & Jones (2012), Palli et al. (2013), Rizzello et al. (2013b), Wilson et al. (2013)). This paper contributes in this direction, providing a performance analysis of a positioning system based on a DEAP under several types of simple feedback control laws. In particular, the model is more general, detailed and accurate with respect to those used in related literature, as it permits to take into account the peculiar geometry of the membrane and it directly incorporates the effects of the mass-spring preloading elements. Moreover, the model is used to develop a number of alternative model-based PID laws (including some nonlinear variants), which are implemented and compared on an experimental bench in a wide range of operative conditions. The resulting study contributes to better assess the actual potentialities and limitations of DEAP as an alternative technology for low cost positioning.

2. DEAP ACTUATOR MODEL

The actuator considered in this work is based on a circular DEAP diaphragm membrane. A sketch of the membrane in the undeformed (a) and deformed (b) condition is shown in Figure 1. The figure introduces also the main geometric parameters. The outer frame and the inner circular plate are made of rigid plastic (green), while the intermediate annular ring is the DEAP silicone membrane (black). The polymeric film is mechanically pre-stretched in the radial direction. Compliant carbon electrodes are printed all over the active area.

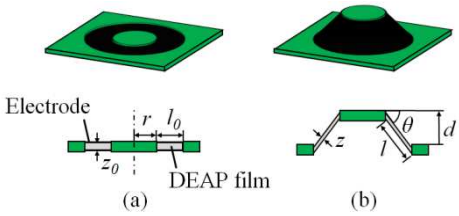

Figure 1. DEAP membrane geometry in the undeformed (a) and deformed configuration (b).

When voltage is applied, an electrically-induced pressure known as Maxwell Stress compresses the membrane in the thickness direction, producing a radial expansion and the subsequent actuation in the out-of-plane direction, as shown in Figure 2. A mass and a linear spring are connected to the moving part of the membrane, and constitute actuator's load. The actuator stroke and force can be tuned by choosing different loading elements.

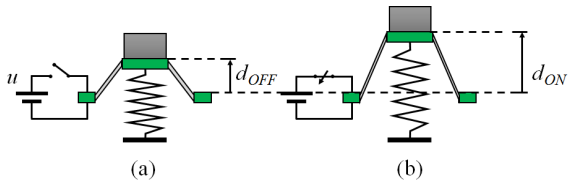

Figure 2. Actuation mechanism, input voltage off (a) and on (b).

A dynamic model of the DEAP-mass-spring system is proposed in this section, based on the work developed in Hodgins et al. (2013). The model describes the relationships between the applied voltage $u(t)$ and the vertical displacement $d(t)$, and is presented here in a condensed form in eq. (1) at the bottom of this page. The state vector is defined as

$$x(t) = \left[\varepsilon_e(t) \quad d(t) \quad \dot{d}(t)\right]^T \tag{2}$$

where ε_e is an internal material strain. In particular, the first equation describes the material viscoelasticity and current deformation state (characterized by ε_e) while the other two equations arise from the forces equilibrium on the biasing mass. Each of the model coefficient $\alpha_i, \beta_i, \gamma_i$ and a_{ij} is obtained as a combination of physical parameters characterizing the system. Note that dependency on the biasing system mass m, the spring stiffness k_s damping η_s and pre-compression d_0, and the gravity acceleration g has been made explicit in (1). For more details on the physics behind the coefficient and the model development, see Hodgins et al. (2013). The term $s(x_2)$ appearing repeatedly in (3) is a nonlinear function of the displacement, defined as follows:

$$s(x_2) = 1 + \frac{x_2^2}{l_0^2} \tag{3}$$

where l_0 is the geometrical parameter defined in Figure 1. Equations (1-3) therefore describe a nonlinear, time-invariant, SISO model that can be used to design feedback controllers, as discussed in the following.

3. PARAMETER IDENTIFICATION AND MODEL VALIDATION

The experimental platform for DEAP actuator testing is shown in Figure 3, and consists of the DEAP membrane together with the mass-spring biasing system, a TREK 610E voltage amplifier, a Keyence LK-G37 laser displacement and a Zaber LA-28A linear actuator connected to the load spring to modify the prestress and apply load disturbances. When recording the system dynamics with a computer-based DAQ system, a first order low-pass filter is included in cascade with the DEAP actuator model in each simulation. The time constant of this filter is estimated to be equal to 6.4 ms. Some of the model parameters are known, namely the ones related to the geometry and the biasing elements. All the parameters describing the material electrical and mechanical properties, instead, require experimental identification. The first identification test aims to characterize the coefficients affecting only the influence the quasi static response, i.e. a_{33}, α_i, β_i and $\gamma_i, i = 1, \ldots, N$. Once force and displacement measurements are available for different voltage levels, stress and strain are reconstructed by means of model equations, and the unknown coefficients are identified by using a LMS algorithm. The results of this

$$\begin{cases} \dot{x}_1 = -a_{11}\left[x_1 - \sqrt{s(x_2)} + 1\right] \\ \dot{x}_2 = x_3 \\ \dot{x}_3 = -\dfrac{k_s}{m}(x_2 - d_0) - \dfrac{\eta_s}{m}x_3 - g - \dfrac{a_{31}}{m}\dfrac{x_2}{s(x_2)}\left\{\displaystyle\sum_{i=1}^{3}\left(\beta_i s(x_2)^{\frac{\alpha_i}{2}} - \gamma_i s(x_2)^{-\frac{\alpha_i}{2}}\right) - a_{32}\left[x_1 - \sqrt{s(x_2)} + 1\right] - a_{33}s(x_2)u^2\right\} \\ y = x_2 \end{cases} \tag{1}$$

identification are summarized in Figure 4. The overlap between the experimental and model behaviors is satisfactory. A small hysteresis introduced by the mechanical behavior of the compliant electrodes is observed between the two variables, but the resulting error seems sufficiently minor to avoid the introduction of further components in the model.

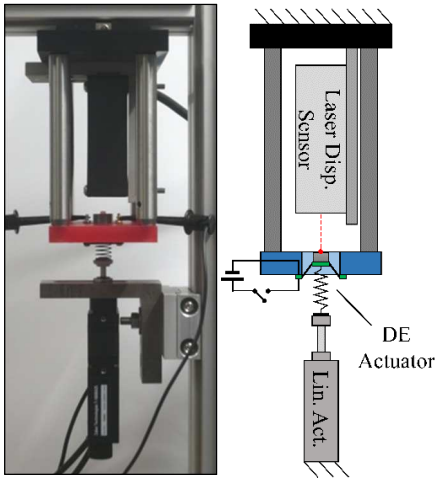

Figure 3. DEAP actuator system, picture (left) and sketch (right).

The remaining model parameters are identified with a Grey-box approach using an Amplitude Modulated Pseudo Random Binary Signal (APRBS) input with a maximum switching frequency of 30 Hz and a duration of 60 seconds. The voltage signal is applied when the actuator is pre-loaded with the spring k_{s2} (Table 1) and a pre-stretch d_0 producing a membrane static pre-deflection of 2 mm. This test permits to identify the viscoelastic model coefficients and the spring damping η_{s2}. The remaining spring damping coefficients η_{s1} and η_{s3} are determined, in conjunction with the previously identified material viscoelastic coefficients, by matching the system response for a square wave input signal. Figure 5 shows results of the system response and the consequent best-fit model response. The identified coefficients values are reported in Table 1. Validation is performed with a sine sweep of linearly increasing frequency from 0 to 50 Hz and a peak amplitude of 1.5 kV, and the results shown in the frequency domain. In particular, Figure 6 shows results for several validation tests, performed for three different springs (see Table 1) and three different membrane pre-deflection for each spring. The model predicts how the natural frequency changes in the range 20 - 45 Hz, when the biasing system is modified.

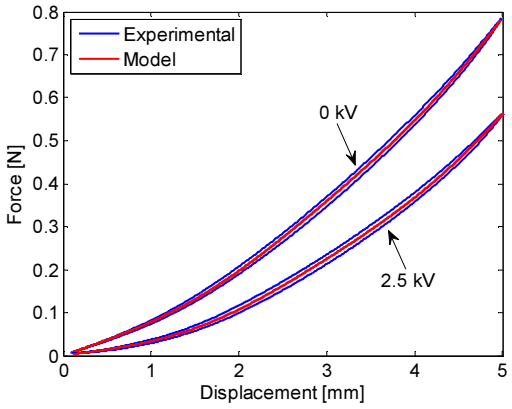

Figure 4. Static model identification, experimental (blue) and model (red).

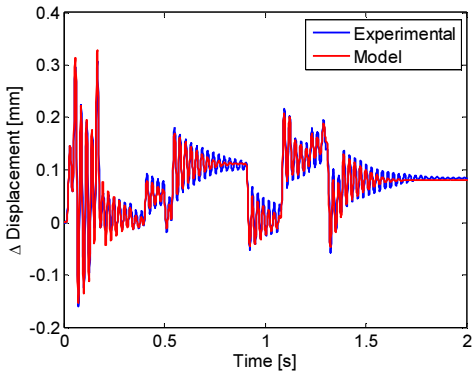

Figure 5. APRBS test, experimental (blue) and model (red).

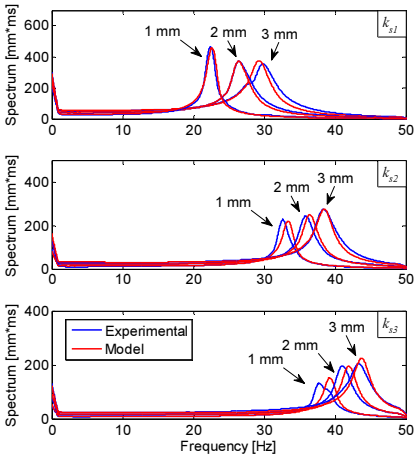

Figure 6. Response spectrum for different springs and DEAP pre-deflections, experimental (blue) and model (red)

Table 1. Model coefficients.

Coefficient	*Value*	*Unit*
g	9.81	m/s^2
m	7.1	g
k_{s1}	0.051	N/mm
k_{s2}	0.22	N/mm
k_{s3}	0.34	N/mm
η_{s1}	$6.48 \cdot 10^{-6}$	$N{\cdot}s/mm$
η_{s2}	$21.86 \cdot 10^{-6}$	$N{\cdot}s/mm$
η_{s3}	$30.48 \cdot 10^{-6}$	$N{\cdot}s/mm$
l_0	4.75	mm
α_1	2	-
α_2	4	-
α_3	6	-
β_1	-7.05	MPa
β_2	3.72	MPa
β_3	-0.54	MPa
γ_1	-17.58	MPa
γ_2	21.06	MPa
γ_3	-7.57	MPa
a_{11}	108.84	$1/s$
a_{31}	0.33	mm
a_{32}	0.48	MPa
a_{33}	0.022	F/m^3

4. CONTROLLERS DESIGN

The control design objective is to obtain a fast and accurate tracking of steps signals of various amplitude. Saturation of control action for long time intervals and chattering must be avoided to prevent excessive stress to the hardware. The desired closed loop transfer function has second order underdamped dynamics characterized by a fixed damping factor $\delta = 0.8$ and a variable natural frequency ω_n used to tune the closed loop time constant τ_{cl}. The design is performed in continuous time, and the implementation is carried out in the digital domain with trapezoid rule and sampling time of 1 ms, and anti-windup algorithms. Design criteria for the considered controllers are discussed in the next subsections. and the final gains of the resulting controllers are summarized in Table 2 at the end of the section.

4.1 Standard PID design

The first controller is a standard linear PID. In order to reduce the high-frequency amplifications introduced by the derivative, the PID controllers is cascaded with a linear first order filter whose time constant τ_f is considered as a further design parameter. The design is based on a linear model of the DEAP actuator obtained by linearization of the model (1-3) around a predefined equilibrium point corresponding to a constant input. Independently of the equilibrium point, the linearized model is characterized by two dominant complex poles, two stable real poles and one minimum phase zero, that is always very close to one pole (the presence of this zero-pole pair can be neglected). Figure 7 shows the Bode diagram for three different voltage levels $\bar{u}$, corresponding to the minimum, intermediate and maximum applied voltage. It can be noted that the static gain of the linearized model decreases for decreasing values of the equilibrium voltage, until the linearized model degenerates in an uncontrollable model for $\bar{u} = 0$.

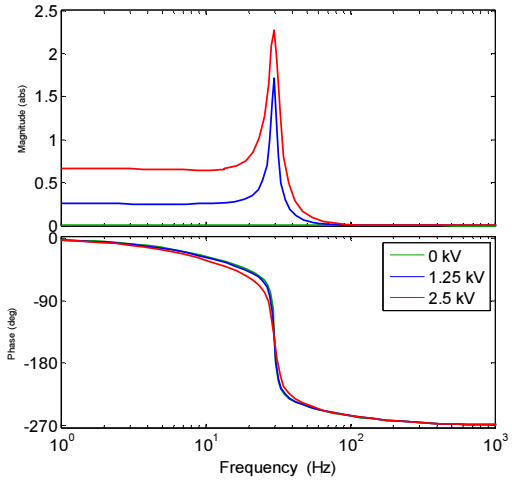

Figure 7. DEAP Linearized model plus sensor low-pass filter bode diagram, different voltages (note the linear scale for the Amplitude diagram).

The free parameters of the PID controller are chosen so that the two zeros of the controller cancel the complex poles of the linearized model, and the residual dynamics leads to a closed loop function with the predefined damping and natural frequency, which is chosen in order to achieve the closed loop time constant τ_{cl} = 56 ms. This control will be hereafter referred to as *PID/TD* (PID designed in Time Domain).

4.2 Nonlinear PID design

Among the various causes of nonlinearity in the DEAP actuator, the analysis of (1-3) reveals that both static and dynamic behaviors of the displacement are influenced by the square of the voltage. A straightforward approach to limit the effects of this nonlinearity is to cancel it by inverse compensation in controller output law. This is obtained with the scheme in Figure 8, in which the controller output is computed as the square root of w, namely the output of the low-pass filtered PID, i.e.

$$u = f(w) = w^{1/2}. \tag{4}$$

The design of the PID law in this case is obtained by considering $f(w)$ as part of the controlled plant, and performing linearization of the dynamics between w and y, and using the same criteria described in the previous subsection to choose the controller gains.

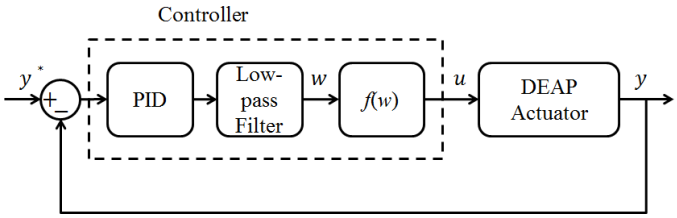

Figure 8. PID plus nonlinear compensation block diagram.

The Bode diagram of the new linearized model, evaluated for different input voltages, is shown in Figure 9. The static nonlinearity cancellation leads to a strong reduction of the differences between the models at various operating points. To better assess the effects of nonlinearity cancellation, the PID is tuned using the same design criterion adopted for the previously described controller (closed loop time constant τ_{cl} = 56 ms). This controller will be referred to as *NPID/TD*. A second version of this controller is also considered in the comparison. More specifically, by hand-tuning, it has been observed that the best tradeoff in terms of closed loop response time, oscillations, and saturation avoidance can be obtained by imposing a closed loop time constant τ_{cl} = 23 ms. This second version of the controller will be referred to as *NPID/TDO* (Nonlinear PID design in Time Domain with Optimized tuning).

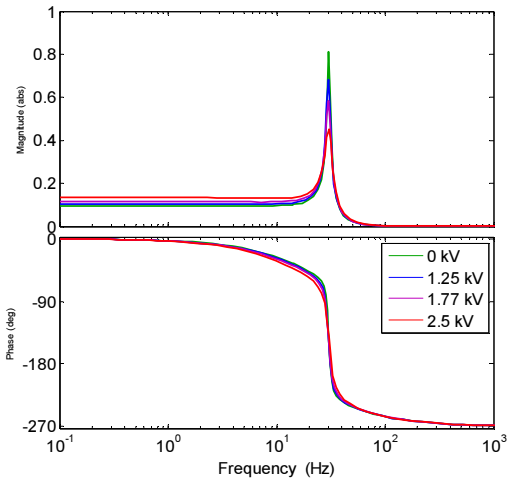

Figure 9. DEAP Linearized model plus nonlinear compensation plus sensor low-pass filter bode diagram bode diagram, different voltages.

4.3 Nonlinear robust PID design

The compensation by inverse cancellation of input nonlinearity contributes to mitigate its effects on the closed loop performance in a wide range of operating point, but it does not provide specific guarantees about the performance degradation caused by the other remaining nonlinearities. A possible way to overcome this limitation is describing the controlled system as a family of linear models, obtained by linearization at various equilibrium points, and using robust control tools to perform the controller design. The method will be applied in conjunction with the static nonlinearity cancellation described in the previous subsection. In particular, in this paper we adopt the direct loop-shaping using small-gain infinity-norm robust control design. The plant is described with the following multiplicative uncertainty description

$$G(s) = \left[1 + \Delta(s) w_i(s)\right] G_n(s) \tag{5}$$

where $G_n(s)$ is the nominal transfer function (obtained by linearization around $\bar{u} = 1.77\ kV$), $w_i(s)$ is a shaping transfer function and $\Delta(s)$ is a random perturbation transfer function such that $\|\Delta(s)\|_\infty < 1$. As $\Delta(s)$ varies, $G(s)$ describes the whole linearized model set. Figure 10 shows a shaping function $w_i(s)$ which includes all the linearized models in the considered voltage range. In order to take into account on unmodeled high frequency uncertainties, the system robustness is tested with an upper bound of the actual $w_i(s)$ (in red in Figure 10).

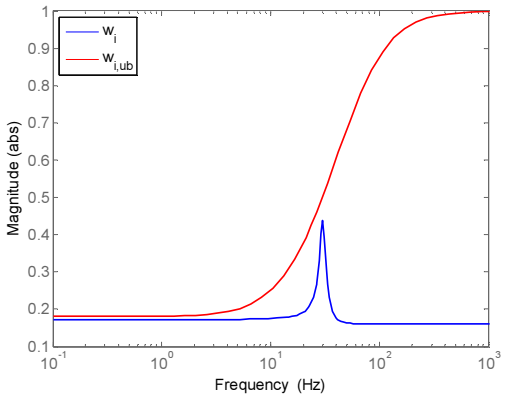

Figure 10. Uncertainty set shaping function (blue) and upper bound (red).

The design criterion consists of properly choosing loop-shaping filters for closed-loop sensitivity and complementary sensitivity in order to guarantee desired closed-loop properties under given model uncertainty, and then solving the design problem with numerical methods (Skogestad & Postlethwaite (2005)). A condition based on the μ-norm upper bound is used in order to establish robust stability and performance of the uncertainty set independently on how fast the function $G(s)$ is perturbed (Shamma (1994)). After preliminary reasoning based on standard robust design criteria the two sensitivity functions shown in Figure 12 are selected as final filters. The H_∞ controller is numerically tuned imposing low-sensitivity bandwidth greater than 3.25 Hz and no resonance peaks in the complementary sensitivity. The resulting H_∞ controller frequency response that is shown in Figure 11, together with low-pass filtered PID approximation of the controller at low frequencies. The sensitivity functions obtained with this controller are shown in Figure 12. This controller will be referred to as *NPID/*H_∞.

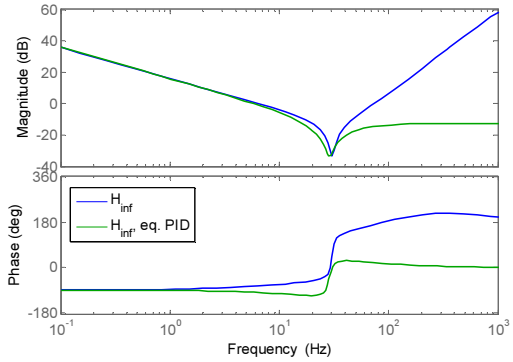

Figure 11. H_∞ controller Bode Diagram, original controller (blue) and low-frequency PID approximation (green).

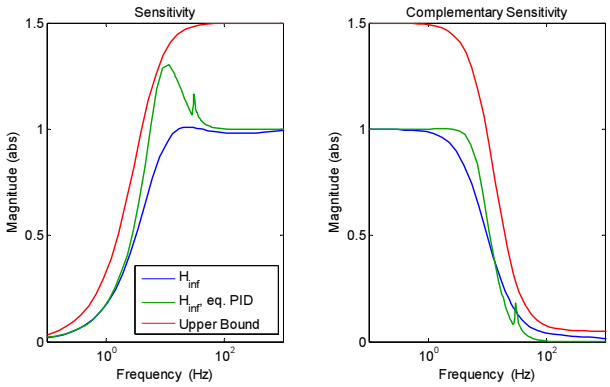

Figure 12. H_∞ Sensitivity (left) and Complementary Sensitivity (right) Bode Diagram, comparison between original controller (blue) and PID approximation (green).

4.4 Sinusoidal tracking with resonant PID control

In addition to the previous controllers which are mainly designed for position regulation, a controller suitable to track harmonic references is considered in this subsection for applications of the DEAP membrane in pumps or other vibrating devices. In order to improve the tracking performance without increasing controller complexity, the following PI-Resonant (PIR) controller is proposed (still applying the nonlinearity compensation of the previous subsection):

$$G_{PIR}(s) = k_p + \frac{k_i}{s} + \frac{k_r s}{s^2 + \omega_r^2} \qquad (6)$$

If ω_r in (6) is set equal to the desired frequency to track, this controller ensures perfect tracking at steady state for a linear plant. If the reference signal is a biased sinewave, the integral term permits also the tracking of the continuous component. This is a consequence of the well-known Internal Model Principle. The controller is tuned with an optimization algorithm that minimizes the 2-norm of the tracking error for the desired reference profile.

Table 2. Controllers coefficients.

PID Controller	k_p	k_i	k_d	τ_f
PID/TD(1.25 kV)	*0.017*	*60.5*	*0.002*	*0.02*
PID/TD(2.5 kV)	*0.013*	*23.6*	*0.001*	*0.02*
NPID/TD(0 kV)	*0.034*	*160*	*0.005*	*0.02*
NPID/TD(1.25 kV)	*0.044*	*151.6*	*0.004*	*0.02*
NPID/TD(1.77 kV)	*0.052*	*138.8*	*0.004*	*0.02*
NPID/TD(2.5 kV)	*0.067*	*118.2*	*0.003*	*0.02*
NPID/TDO(1.77 kV)	*0.12*	*321.7*	*0.009*	*0.005*
NPID/H_∞(1.77 kV)	*0.27*	*366.3*	*0.011*	*0.005*
PIR Controller	k_p	k_i	k_r	ω_r
NPIR(5 Hz, 1.77 kV)	*-5.81*	*53.4*	*66.3*	*5·2π*
NPIR(15 Hz, 1.77 kV)	*-0.867*	*211.5*	*196*	*15·2π*

5. SIMULATION AND EXPERIMENTAL RESULTS

This section summarizes the experimental results of the controllers described in the previous section. The experimental setup is the same used for model identification and shown in Figure 3. The results of the *PID/TD* is shown in Figure 13, for $\bar{u} = 1.25\ kV$. The response of this controller is satisfactory if the system operates in the neighborhoods of the equilibrium point, and it becomes excessively under or overdamped in other regions due to system nonlinearities. Similar results are obtained by tuning the controller on different equilibrium points. The figure also compares the simulated and experimental closed loop performances, showing a good agreement between the signals. Figure 14 shows the performance of the *NPID/TDO* controller. The effect of this compensation on the control performance appear very clear in the figure. The response of the optimized PID is also very close to the one obtained with the H_∞ design, shown in Figure 15. In the tracking error plot in Figure 15, a curve labeled as "bound" appears, and corresponds to the response of the performance matrix producing a μ-norm upper bound smaller than 1 (robust performance condition). The tracking error converges to zero always faster than this signal. A comparison of tracking error for the controllers is reported in Figure 16. Experimental results for a disturbance rejection test for *NPID/TDO* and *NPID/H_∞* are shown in Figure 17. The linear actuator is moved at constant velocity to a desired final position, simulating a load disturbance, which is efficiently compensated by the control system. Finally, the performance of the NPIR control for a 15 Hz reference is shown in Figure 18. When a sine sweep reference is applied, the tracking error reaches its minimum when the input is at the resonance frequency ω_r, proving the effectiveness of the proposed strategy. The steady-state error peak is 14.89 µm. Table 3 summarizes the main performance indices of the considered controllers. Indices are the 2-norm of the tracking error, the average steady state error and the average steady state error when the input saturation occurs. The quantity in brackets represents the equilibrium voltage of the linearized plant used for the design. *NPID/H_∞* shows the best performance in terms of all the proposed indices.

NPID/TDO on the other hand performs very close to *NPID/H∞*, which is much more demanding in terms of manual and numerical design effort.

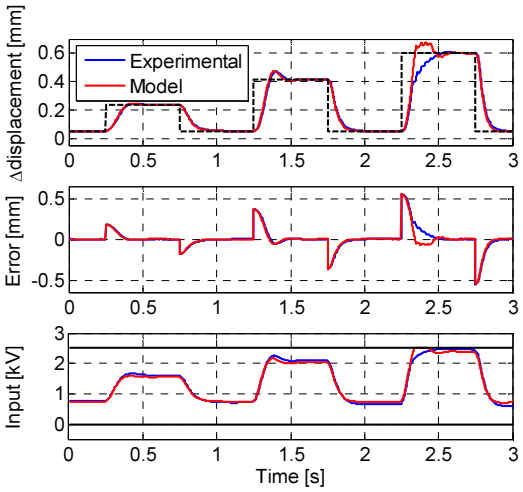

Figure 13. *PID/TD*, tuned on the linearized model at 1.25 kV.

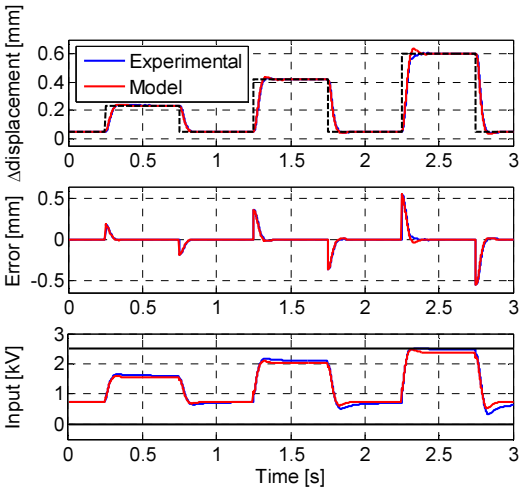

Figure 14. *NPID/TDO*, with nonlinearity compensation, tuned on the linearized model at 1.77 kV, optimized tuning.

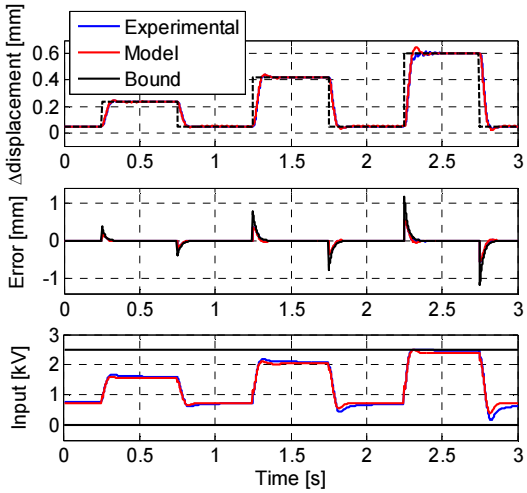

Figure 15. *NPID/H∞*, with nonlinearity compensation, tuned on the linearized model at 1.77 kV.

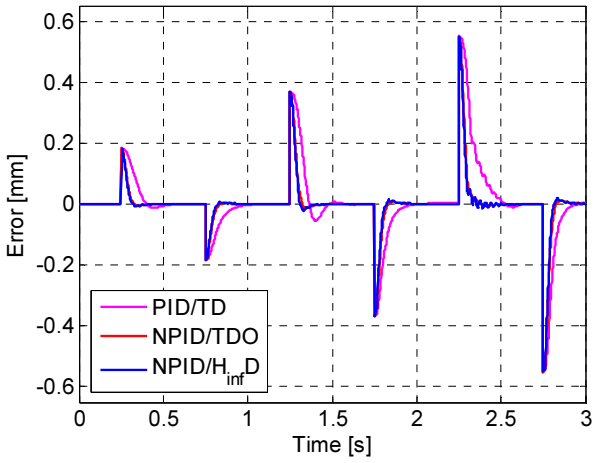

Figure 16. Tracking error comparison for different controllers, experimental results.

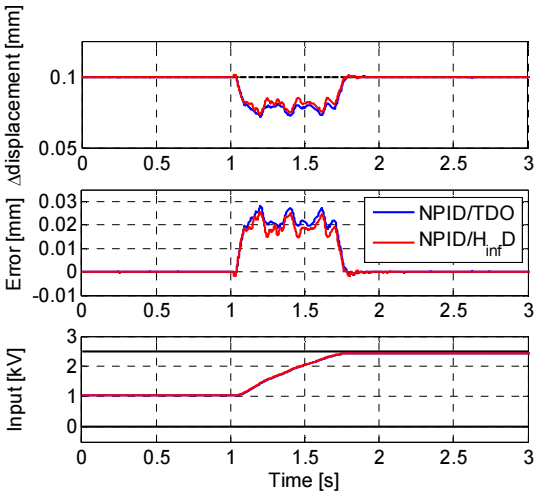

Figure 17. Disturbance rejection comparison, experimental results, *NPID/TDO* and *NPID/H∞*.

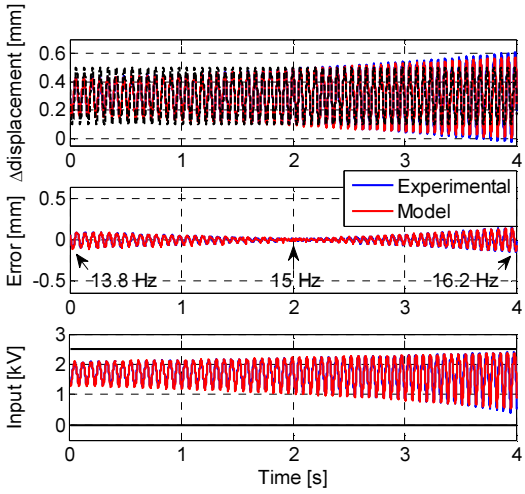

Figure 18. *NPIR*, with nonlinearity compensation, Sine sweep input around 15 Hz.

Table 3. PID Controllers performance.

Controller	$\|e\|_2$	$mean(e_{ss})$	$mean(e_{ss,sat})$
PID/TD(1.25 kV)	*6.87*	*0.48 μm*	*0.75 μm*
PID/TD(2.5 kV)	*9.06*	*8.77 μm*	*4.59 μm*
NPID/TD(0 kV)	*6.89*	*0.09 μm*	*1.62 μm*
NPID/TD(1.25 kV)	*7.07*	*0.04 μm*	*1.84 μm*
NPID/TD(1.77 kV)	*7.24*	*0.09 μm*	*2.19 μm*
NPID/TD(2.5 kV)	*7.67*	*0.25 μm*	*3.07 μm*
NPID/TDO(1.77 kV)	*4.92*	*0.06 μm*	*0.68 μm*
NPID/H_∞(1.77 kV)	*4.65*	*0.05 μm*	*0.57μm*

6. CONCLUSIONS

This paper has discussed a number of alternative design strategies for position controllers of a DEAP electro-mechanical actuator. All of the design strategies take advantage of a detailed, nonlinear model of the system, which can be used to either perform linear design by means of linearization, or to identify and compensate the main sources of nonlinearity. The experimental comparison reveals that the second strategy is significantly more effective, and leads to the best controllers for the actuator, both in terms of tracking error and disturbance rejection. The nonlinearity cancellation can be combined with other robust control design tool, such as H_∞ approaches in the frequency domain, to obtain accurate tracking performance along with a useful characterization of the effects of the residual uncertainties in the model. The case of sinusoidal reference tracking is satisfactorily addressed with another variant of the PID with a resonant term. In conclusion, the reasoned use of well-tuned linear strategies permits to obtain satisfactory performances on the particular type of DEAP actuator considered in the paper. Further works include the use of computational intelligence tools (Cupertino et al. 2003) to automatically design nonlinear controllers to reduce the error peaks during transients without generating chattering or saturation. Other more advanced versions of the actuator use further nonlinear components, such as bistable springs, to obtain larger deformations with the same voltage range. The introduction of these components make the need of nonlinear control design even more suitable, and also this issue is among the main directions for further work.

REFERENCES

Berselli, G. et al., (2012). Dynamic modeling and experimental evaluation of a constant-force dielectric elastomer actuator. Journal of Intelligent Material Systems and Structures, 24(6), pp.779–791.

Cupertino, F., Giordano, V., Naso, D., Turchiano, B., Salvatore, L. (2003). On-line genetic design of fuzzy controllers for DC drives with variable load. *Electronic Letters*, Vol. 39, n. 5, pp. 479-480.

Giousouf, M., Kovacs, G. (2013). Dielectric elastomer actuators used for pneumatic valve technology. Smart Mater. Struct., vol. 22, no. 10, p. 104010, Oct. 2013.

Hackl, C.M. et al., (2005). A Multidomain Model of Planar Electro-Active Polymer Actuators. IEEE Transactions on Industry Applications, 41(5), pp.1142–1148.

Hodgins, M. et al., (2013). High-Frequency Dynamic Model of a Pre-Loaded Circular Dielectric Electro-Active Polymer Actuator. Proceedings of the ASME 2013 Conference on Smart Materials, Adaptive Structures and Intelligent Systems SMASIS2013, pp.1–10.

Hodgins, M., York, A. & Seelecke, S. (2011). Modeling and experimental validation of a bi-stable out-of-plane DEAP actuator system. Smart Materials and Structures, 20(9), p.094012.

Jordan, G., McCarthy, D. N., Schlepple, N., Krißler, J., Schröder, H., and Kofod, G. (2011). Actuated Micro-optical Submount Using a Dielectric Elastomer Actuator. IEEE/ASME Transactions on Mechatronics, vol. 16, no. 1, pp. 98–102.

Kaal, W. & Herold, S. (2011). Electroactive Polymer Actuators in Dynamic Applications. IEEEASME Transactions on Mechatronics, 16(1), pp.24–32.

Loverich, J. J., Kanno, I., and Kotera, H. (2006). Concepts for a new class of all-polymer micropumps. Lab Chip, vol. 6, no. 9, pp. 1147–54, Sep. 2006.

Plante, J. & Dubowsky, S., (2007). On the performance mechanisms of Dielectric Elastomer Actuators. Sensors and Actuators A: Physical, 137(1), pp.96–109.

Plante, J. (2006). Dielectric Elastomer Actuators for Binary Robotics and Mechatronics. Massachusetts Institute of Technology, 2006, pp.1-186.

Randazzo, M. et al., (2010). Closed loop control of a rotational joint driven by two antagonistic dielectric elastomer actuators. Proc. SPIE 7642, Electroactive Polymer Actuators and Devices (EAPAD) 2010, 76422D.

Rizzello, G. et al., (2013a). A Nonlinear Electro-Mechanical Model for an Annular Dielectric Elastomer Actuator with a Biasing Mass. Mechatronik 2013, Aachen, March, 06-08, 2013.

Rizzello, G. et al., (2013b). Modeling and Position Control of an Electromechanical Actuator Based on a Mass-Spring-Biased EAP System. ETFA2013, Cagliari, 11-13 September 2013.

Sarban, R. & Jones, R.W., (2012). Physical model-based active vibration control using a dielectric elastomer actuator. Journal of Intelligent Material Systems and Structures, 23(4), pp.473–483.

Shamma, J., (1994). Robust stability with time-varying structured uncertainty. IEEE Transactions on Automatic Control, Vol. 39, No. 4.

Skogestad, S. & Postlethwaite, I., (2005). Multivariable feedback control: analysis and design. John Wiley & Sons.

Wilson, E.D. et al., (2013). Bioinspired Adaptive Control for Artificial Muscles. , pp.311–322.

Wissler, M. & Mazza, E., (2007). Mechanical behavior of an acrylic elastomer used in dielectric elastomer actuators. Sensors and Actuators A: Physical, 134(2), pp.494–504.

Xie, S.Q. et al., (2005). An Adaptive Control System for Dielectric Elastomers. 2005 IEEE International Conference on Industrial Technology, pp.335–340.

York, A., Dunn, J. & Seelecke, S., (2010). Experimental characterization of the hysteretic and rate-dependent electromechanical behavior of dielectric electro-active polymer actuators.